Monthly Notices
of the
ROYAL ASTRONOMICAL SOCIETY

Mon. Not. R. Astron. Soc. **415,** 2336–2348 (2011) doi:10.1111/j.1365-2966.2011.18864.x

Herschel-ATLAS: first data release of the Science Demonstration Phase source catalogues

E. E. Rigby,[1⋆] S. J. Maddox,[1] L. Dunne,[1] M. Negrello,[2] D. J. B. Smith,[1] J. González-Nuevo,[3] D. Herranz,[4] M. López-Caniego,[4] R. Auld,[5] S. Buttiglione,[6] M. Baes,[7] A. Cava,[8] A. Cooray,[9] D. L. Clements,[10] A. Dariush,[5] G. De Zotti,[3,6] S. Dye,[5] S. Eales,[5] D. Frayer,[11] J. Fritz,[7] R. Hopwood,[2] E. Ibar,[12] R. J. Ivison,[12,13] M. Jarvis,[14] P. Panuzzo,[15] E. Pascale,[5] M. Pohlen,[5] G. Rodighiero,[6] S. Serjeant,[2] P. Temi[16] and M. A. Thompson[14]

[1]*School of Physics and Astronomy, University of Nottingham, University Park, Nottingham NG7 2RD*
[2]*Department of Physics and Astronomy, The Open University, Walton Hall, Milton Keynes MK7 6AA*
[3]*SISSA, Via Bonomea 265, I-34136 Trieste, Italy*
[4]*Instituto de Física de Cantabria (CSIC-UC), Avda. los Castros s/n, 39005 Santander, Spain*
[5]*School of Physics and Astronomy, Cardiff University, The Parade, Cardiff CF24 3AA*
[7]*Sterrenkundig Observatorium, Universiteit Gent, Krijgslaan 281 S9, B-9000 Gent, Belgium*
[6]*INAF Osservatorio Astronomico di Padova, Vicolo Osservatorio 5, I-35122 Padova, Italy*
[8]*Departamento de Astrofísica, Facultad de CC. Físicas, Universidad Complutense de Madrid, E-28040 Madrid, Spain*
[9]*Department of Physics and Astronomy, University of California, Irvine, CA 92697, USA*
[10]*Astrophysics Group, Imperial College, Prince Consort Road, London SW7 2AZ*
[11]*Infrared Processing and Analysis Center, California Institute of Technology 100-22, Pasadena, CA 91125, USA*
[12]*UK Astronomy Technology Centre, Royal Observatory Edinburgh, Edinburgh EH9 3HJ*
[13]*Institute for Astronomy, University of Edinburgh, Royal Observatory, Edinburgh EH9 3HJ*
[14]*Centre for Astrophysics, Science & Technology Research Institute, University of Hertfordshire, Hatfield, Herts AL10 9AB*
[15]*Centre CEA de Saclay (Essonne), Gif-sur-Yvette, 921191 Cedex, France*
[16]*Astrophysics Branch, NASA Ames Research Center, Mail Stop 245-6, Moffett Field, CA 94035, USA*

Accepted 2011 April 5. Received 2011 March 30; in original form 2010 October 22

ABSTRACT

The *Herschel* Astrophysical Terahertz Large Area Survey (*Herschel*-ATLAS) is a survey of 550 deg^2 with the *Herschel* Space Observatory in five far-infrared and submillimetre bands. The first data for the survey, observations of a field 4×4 deg^2 in size, were taken during the Science Demonstration Phase (SDP), and reach a 5σ noise level of 33.5 mJy beam^{-1} at 250 μm. This paper describes the source extraction methods used to create the corresponding SDP catalogue, which contains 6876 sources, selected at 250 μm, within ∼14 deg^2. Spectral and Photometric Imaging REciever (SPIRE) sources are extracted using a new method specifically developed for *Herschel* data and Photodetector Array Camera and Spectrometer (PACS) counterparts of these sources are identified using circular apertures placed at the SPIRE positions. Aperture flux densities are measured for sources identified as extended after matching to optical wavelengths. The reliability of this catalogue is also discussed, using full simulated maps at the three SPIRE bands. These show that a significant number of sources at 350 and 500 μm have undergone flux density enhancements of up to a factor of ∼2, due mainly to source confusion. Correction factors are determined for these effects. The SDP data set and corresponding catalogue will be available from www.h-atlas.org.

Key words: methods: data analysis – catalogues – surveys – galaxies: general – submillimetre: galaxies.

1 INTRODUCTION

The *Herschel*-Astrophysical Terahertz Large Area Survey (H-ATLAS) is the largest, in time and area, of the extragalactic

⋆E-mail: emma.rigby@nottingham.ac.uk; emmaerigby@gmail.com

Open Time Key Projects to be carried out with the European Space Agency (ESA) *Herschel* Space Observatory (Pilbratt et al. 2010).[1] When complete it will cover ∼550 deg^2 of the sky, in five far-infrared and submillimetre bands (100, 160, 250, 350 and 500 μm), to a 5σ depth of 33 mJy beam^{-1} at 250 μm. The predicted number of sources is ∼200 000; of these ∼40 000 are expected to lie within $z < 0.3$. A full description of the survey can be found in Eales et al. (2010).

This paper presents the 250 μm selected source catalogue created from the initial H-ATLAS Science Demonstration Phase (SDP) observations. Eight papers based on this catalogue have already been published in the *Astronomy and Astrophysics Herschel* Special Issue ranging from the identification of blazars (González-Nuevo et al. 2010) and debris discs (Thompson et al. 2010) in the SDP field, to determinations of the colours (Amblard et al. 2010), source counts (Clements et al. 2010), clustering (Maddox et al. 2010) and 250 μm luminosity function evolution (Dye et al. 2010) of the submillimetre population, as well as the star formation history of quasar host galaxies (Serjeant et al. 2010) and the dust energy balance of a nearby spiral galaxy (Baes et al. 2010).

The layout of the paper is as follows. Section 2 describes the SDP observations; Section 3 describes the source extraction procedure for the five bands and, finally, Section 4 outlines the simulations used to quantify the reliability of the catalogue. For more details of the SDP data, see Pascale et al. (2011) and Ibar et al. (2010) for the Spectral and Photometric Imaging REciever (SPIRE) and Photodetector Array Camera and Spectrometer (PACS) data reduction, respectively, and Smith et al. (2011) for the multi-wavelength catalogue matching.

2 *HERSCHEL* OBSERVATIONS

The SDP observations for the H-ATLAS cover an area of ∼4° × 4°, centred at $\alpha = 09^{\rm h}05^{\rm m}30\overset{\rm s}{.}0$, $\delta = 00^\circ30'00\overset{''}{.}0$ (J2000). This field lies within one of the regions of the Galaxy and Mass Assembly (GAMA) survey (Driver et al. 2009) so optical spectra, along with additional multi-wavelength data, are available for the majority of the low-redshift sources.

The observations were taken in parallel mode, which uses the PACS (Poglitsch et al. 2010) and SPIRE (Griffin et al. 2010) instruments simultaneously; two orthogonal scans were used to mitigate the effects of $1/f$ noise. The time-line data were reduced using HIPE (Ott et al. 2010). SPIRE 250, 350 and 500 μm maps were produced using a naïve mapping technique, after removing any instrumental temperature variations (Pascale et al. 2011), and incorporating the appropriate flux calibration factors. Noise maps were generated by using the two cross-scan measurements to estimate the noise per detector pass, and then for each pixel the noise is scaled by the square root of the number of detector passes. The SPIRE point spread function (PSF) for each band was determined from Gaussian fits to observations of Neptune, the primary calibrator for the instrument. Maps from the PACS 100 and 160 μm data were produced using the PhotProject task within HIPE (Ibar et al. 2010). A false colour-combined image of a part of the three SPIRE maps is shown in Fig. 1. The measured beam full width at half-maxima (FWHMs) are approximately 9 arcsec, 13 arcsec, 18 arcsec, 25 arcsec and 35 arcsec for the 100, 160, 250, 350 and 500 μm bands, respectively (Ibar et al. 2010; Pascale et al. 2011). The map pixels are 2.5 arcsec, 5 arcsec, 5 arcsec, 10 arcsec and 10 arcsec in size for the same five bands.

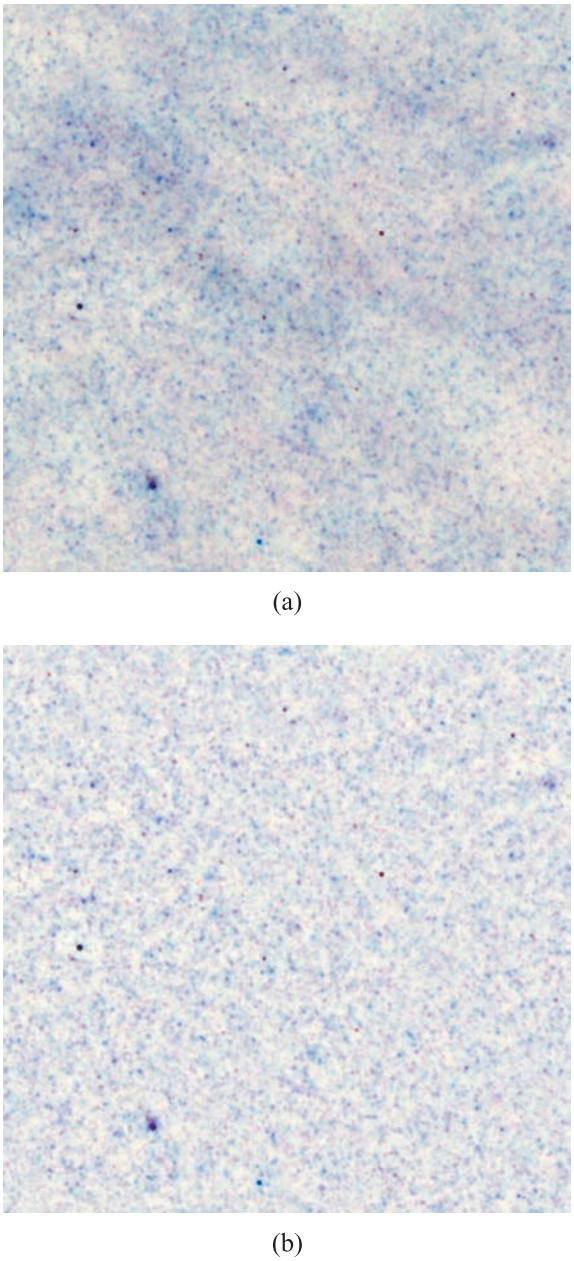

(a)

(b)

Figure 1. False-colour images of a 1.5 deg^2 region of the SDP field showing the three SPIRE bands combined: (a) original combined map, (b) after background subtraction. Image (a) is before background-subtraction and shows clear contamination by galactic cirrus; image (b) shows the reduction in contamination after subtracting the background.

The noise levels measured by Pascale et al. (2011) for the 250 and 500 μm SPIRE bands are in good agreement with those predicted using the *Herschel* Space Observatory Planning Tool (HSpot[2]); for the 350 μm band they are considerably better. The corresponding PACS noise levels determined by Ibar et al. (2010) are currently

[1] *Herschel* is an ESA space observatory with science instruments provided by European-led Principal Investigator consortia and with important participation from NASA.

[2] HIPE and HSpot are joint developments by the Herschel Science Ground Segment Consortium, consisting of ESA, the NASA Herschel Science Center, and the HIFI, PACS and SPIRE consortia.

higher than predicted (26 and 24 mJy, compared with 13.4 and 18.9 mJy for 100 and 160 μm, respectively), but this may improve in future with better map-making techniques. The flux calibration uncertainties are 15 per cent for the three SPIRE bands (Pascale et al. 2011) and 10 and 20 per cent for the PACS 100 and 160 μm bands, respectively (Ibar et al. 2010).

3 SOURCE EXTRACTION

The ultimate aim for the source identification of the H-ATLAS data is to use a multi-band method to perform extraction across the five wavebands simultaneously, thus utilizing all the available data as well as easily obtaining complete flux density information for each detected galaxy, without having to match catalogues between bands. However, the short time-scale for the reduction of these SDP observations, combined with the higher than expected PACS noise levels, means that this was only possible for the three SPIRE bands. As a result, the source extraction for the PACS and SPIRE maps is discussed separately in this section.

The full H-ATLAS SDP catalogue described here will be available at http://www.h-atlas.org.

3.1 The SPIRE catalogue

Sources are identified in the SPIRE 250, 350 and 500 μm maps using the Multi-band Algorithm for source eXtraction (MADX; Maddox et al. in preparation), which is being developed for the H-ATLAS. Several methods for generating the final SPIRE catalogue with MADX were investigated and these are described below.

The first step in the MADX source extraction is to subtract a local background, estimated from the peak of the histogram of pixel values in 30 × 30 pixel blocks (chosen to allow the map to be easily divided up into independent sub-regions). This corresponds to 2.5 × 2.5 arcmin^2 for the 250 μm map, and 5 × 5 arcmin^2 for the 350 and 500 μm maps. The background (in mJy beam^{-1}) at each pixel was then estimated using a bi-cubic interpolation between the coarse grid of backgrounds, and subtracted from the data. Fig. 1 illustrates the reduction in background contamination (mainly arising from galactic cirrus, which dominates over the confusion noise from unresolved sources) obtained using this method.

The background-subtracted maps were then filtered by the estimated PSF, including an inverse variance weighting, where the noise for each map pixel was estimated from the noise map (matched filtering; e.g. Turin 1960; Serjeant et al. 2003). The background removal has a negligible effect on the PSF because the histogram peak is insensitive to resolved sources in the background aperture; this will be discussed further in Maddox et al. (in preparation). We also create a 'filtered noise' map which represents the noise on a pixel in the PSF filtered map. This is lower than the raw noise map because the noise in the SPIRE pixels is uncorrelated, and so filtering by the PSF reduces the noise by approximately the square root of the number of pixels per beam.

The maps from the 350 and 500 μm bands are interpolated on to the 250 μm pixels. Then all three maps are combined with weights set by the local inverse variance, and the prior expectation of the spectral energy distribution (SED) of the galaxies. We used two SED priors: a flat-spectrum prior (assumed to be flat in f_ν), where equal weight is given to each band, and also 250 μm weighting, where only the 250 μm band was included.

Local, $>2.5\sigma$, peaks are identified in the combined PSF filtered map as potential sources, and sorted in order of decreasing significance level. A Gaussian is fitted to each peak in turn to provide an estimate of the position at the sub-pixel level; this can be influenced by the presence of a neighbouring source, as illustrated in Fig. 2,

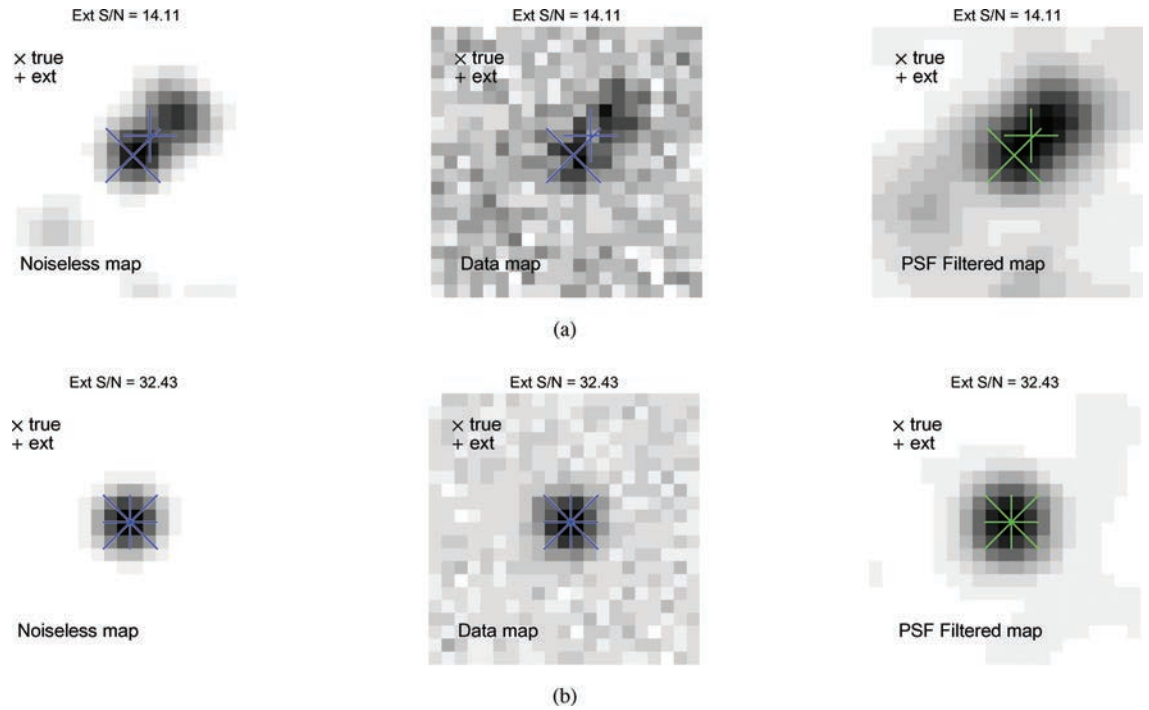

Figure 2. The input (true) and extracted position for two point sources in the 250 μm simulated maps before the addition of Gaussian noise (noiseless), after the noise has been added (noisy) and after further convolving with the 250 μm PSF to create the final realistic sky (PSF-filtered) (see Section 4 for full details), to illustrate how the position, and therefore flux density, of an extracted source found by MADX can be influenced by the presence of a close companion: (a) source with a close companion, (b) isolated source.

but the effect is minimal. The flux in each band is then estimated using a bi-cubic interpolation to the position given by the combined map. The scaled PSF is then subtracted from the map before going on to the next source in the sequence. This ensures that flux from the wings of bright sources does not contaminate nearby fainter sources. This sorting and PSF subtraction reduce the effect of confusion, but in future releases we plan to implement multi-source fitting to blended sources.

To produce a catalogue of reliable sources, a source is only included if it is detected at a significance of at least 5σ in one of the SPIRE bands. The total number of sources in the SPIRE catalogue is 6876.

For our current data we chose to use the 250 μm only prior for all our catalogues, which means that sources are identified at 250 μm only. At the depth of the filtered maps source confusion is a significant problem, and the higher resolution of the 250 μm maps outweighed the signal-to-noise ratio (S/N) gain from including the other bands (see Section 4.1 and Fig. 8c). This may introduce a bias in the catalogue against red, potentially high redshift, sources that are bright at 500 μm, but weak in the other bands. However, comparing catalogues made with both the 250 μm and flat-spectrum priors showed that the number of missed sources is low: 2974 $> 5\sigma$ 350 μm sources and 348 $> 5\sigma$ 500 μm sources are detected with the flat prior, compared with 2758 and 307 sources detected using the 250 μm prior (i.e. 7 and 12 per cent of sources are missed at 350 and 500 μm, respectively). It should also be noted that for a high-redshift source to be missed it would need a 500 to 250 μm flux ratio of >2.7 (i.e. it has to be $<2.5\sigma$ at 250 μm to be excluded from the catalogue). Assuming typical SED templates (e.g. M82 and Arp 220), this means that this should only occur for sources which lie at redshifts >4.6. We aim to revisit this issue in future data releases.

Since MADX uses a bicubic interpolation to estimate the peak flux in the PSF filtered map, it partially avoids the peak suppression caused by pixelating the time-line data, as discussed by Pascale et al. Nevertheless, the peak fluxes are systematically underestimated, and so pixelization correction factors were calculated by pixelating the PSF at a large number of random sub-pixel positions. The mean correction factors were found to be 1.05, 1.11 and 1.04 in the 250, 350 and 500 μm bands, respectively, and they have been included in the released SDP catalogue.

In calculating the σ for each source, we use the filtered noise map and add the confusion noise to this in quadrature. The average 1σ instrumental noise values are 4.1, 4.0 and 5.7 mJy beam^{-1}, respectively, with 5 per cent uncertainty, in the 250, 350 and 500 μm bands, determined from the filtered maps (Pascale et al. 2011). We estimated the confusion noise from the difference between the variance of the maps and the expected variance due to the instrumental noise (assuming that confusion is dominating the excess noise), and find that the 1σ confusion noise is 5.3, 6.4 and 6.7 mJy beam^{-1} at 250, 350 and 500 μm, with an uncertainty of 7 per cent; these values are in good agreement with those found by Nguyen et al. (2010) using data from the Herschel Multi-tiered Extragalactic Survey (HerMES). The resulting average 5σ limits are therefore 33.5, 37.7 and 44.0 mJy beam^{-1}.

3.1.1 Extended sources

The flux density extracted by MADX will underestimate the true value for sources that are larger than the SPIRE beams, which have FWHM of 18.1 arcsec, 24.8 arcsec and 35.2 arcsec for 250, 350 and 500 μm, respectively. This occurs because the peak value taken by MADX only accurately represents the true flux density of a source if it is point like. These extended sources can be identified if they also have a reliable optical match and therefore a corresponding optical size, $r_{\rm opt}$ (equivalent to the 25 mag arcsec^{-2} isophote), in the Sloan Digital Sky Survey or GAMA catalogues [see Smith et al. (2011) for full details of the matching procedure and the determination of the match reliability, R_j]. The size of the aperture used is listed in the catalogue, and the most appropriate flux density, either point source or aperture measurement (when this is larger), is given for each source in the SPIRE 'BEST flux' columns. It should be noted that, apart from two exceptions, this is necessary at 250 and 350 μm only, as the large 500 μm beam size means that the flux discrepancy is negligible for that map.

An 'extended source', in a particular map, is defined here as one with $r_{\rm opt} > 0.5\times$ FWHM, and to ensure only true matches are used, it must also have a match-reliability, R_j, greater than 0.8. In total, the MADX 'BEST' flux columns for 167 sources at 250 μm and 53 sources at 350 μm were updated with aperture photometry values.

The aperture radius, $a_{\rm r}$, in a particular band is set by summing the optical size in quadrature with the FWHM of that band:

$$a_{\rm r} = \sqrt{\rm FWHM^2 + r_{opt}^2}. \quad (1)$$

The exceptions to this were the apertures used for sources H-ATLAS J091448.7−003533 (a merger, where the given $a_{\rm r}$ is insufficient to include the second component) and H-ATLAS J090402.9+005436, which visual inspection showed was clearly extended. In these cases the aperture sizes used are chosen to match the extent of the sub-mm emission, and fluxes are replaced in the 500 μm band as well.

The apertures are placed on the MADX, Jy beam^{-1}, background-subtracted maps, at the catalogue position for each source; the measured values are converted to the correct flux scale by dividing by the area of the beam derived by Pascale et al. (2011) for each map (13.9, 6.6 or 14.2 pixels for 250, 350 and 500 μm, respectively). The corresponding 1σ error is given by $\sqrt{v_{\rm ap}}$, where $v_{\rm ap}$ is the sum of the variances within apertures placed in the same positions on the relevant variance maps. Confusion noise estimates were again added in quadrature to these uncertainties; these were scaled according to the area of each individual aperture.

Fig. 3 compares the MADX and aperture-measured fluxes for all catalogue sources with a possible optical identification. It shows that the majority of objects are point like, for which the agreement between the two sets of fluxes is good. The sources identified as extended are highlighted in bold, and it is clear that MADX underestimates these at 250 and 350 μm if they are brighter than ∼100 mJy.

3.2 The PACS catalogue

The higher noise levels in the PACS maps, along with the shape of the source SEDs, mean that all the PACS extragalactic sources should be clearly detected in the SPIRE catalogue. Sources in the PACS data are therefore identified by placing circular apertures at the SPIRE 250 μm positions in the 100 and 160 μm maps, after correcting the PACS astrometry to match that of the 250 μm map (using the sources present in both the SPIRE and PACS maps). There are two steps to this source detection process: first a 'point source' measurement is obtained for all SPIRE positions using apertures with radii of 10 arcsec (100 μm) or 15 arcsec (160 μm); next additional aperture fluxes are found for positions where a PACS source would satisfy the extended source criteria discussed in Section 3.1.1. Aperture radii in this case are calculated using equation (1), assuming FWHM of 8.7 and 13.1 arcsec for 100 and 160 μm, respectively.

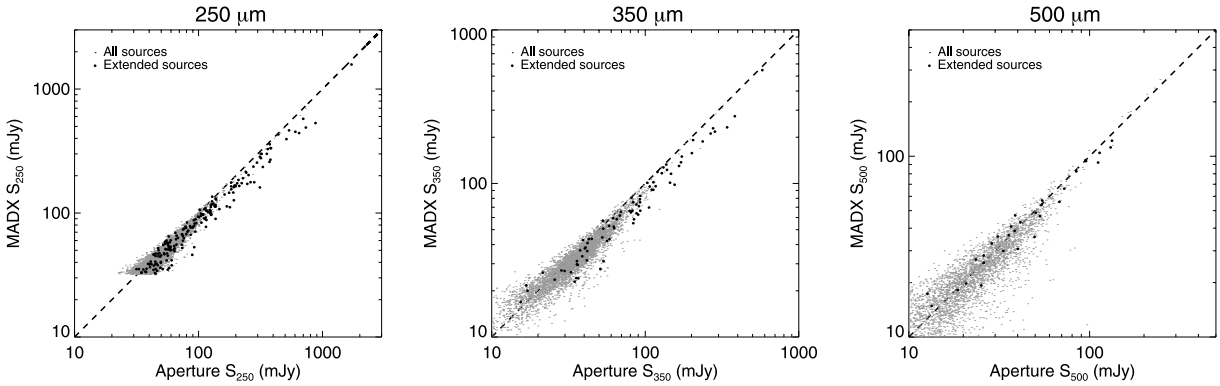

Figure 3. A comparison between the MADX and aperture-measured fluxes for the sources with a possible optical identification in the matched catalogue of Smith et al. (2011). Sources identified as extended are highlighted in bold.

These FWHM values are calculated using rough modelling of the Vesta asteroid as the full PACS PSFs are asymmetric (see Ibar et al. 2010, for a full discussion).

The aggressive filtering used for these maps means that the large-scale structure in the cirrus has already been removed, but some noise stripes remain. These are removed globally at 160 μm by subtracting a background determined within 10 × 10 pixel blocks. However, at 100 μm this global approach was found to introduce negative holes around bright sources so the background value is determined for each source individually using a local annulus with a width of 0.5 times the aperture radius.

Unlike SPIRE, the PACS maps have units of Jy pixel^{-1} so no beam conversion is needed. However, the fluxes are divided by 1.09 (100 μm) or 1.29 (160 μm) as recommended by the PACS Instrument Control Centre.[3] These scaling factors are now incorporated into the data-reduction pipeline and have been applied to the public release of the PACS SDP maps, along with the astrometry correction needed to match that of the SPIRE 250 μm map (this correction is ∼1 arcsec in both PACS bands). The fluxes are also aperture corrected, using a correction determined from observations of a bright point-like source. The 1σ errors are found using apertures randomly placed in the maps; note that these errors scale with aperture size. The low confusion noise compared to SPIRE, plus the fast scan speed used in these observations, means that the integration time used in H-ATLAS is insufficient to provide confusion limited images with PACS. Full details of these observations can be found in Ibar et al. (2010).

The most appropriate flux density measurements, either point or extended (where this is larger), are given in the 'BEST' PACS columns in the SDP catalogue, along with the corresponding aperture radii, for sources with S/N $\geq$ 5. As a result 151 and 304 sources satisfy this condition at 100 and 160 μm, respectively. The 5σ point source limits in the PACS catalogue are 132 and 121 mJy at 100 and 160 μm. It should be noted that the flux densities extracted from the PACS maps are only at 100 and 160 μm under the assumption of a constant energy spectrum, though the colour corrections for sources with a different SED are small (Poglitsch et al. 2010).

The PACS time-line data have been high-pass filtered by subtracting a boxcar median over 3.4 arcmin (at 100 μm) and 2.5 arcmin at 160μm (Ibar et al. 2010). The filtering will lead to the underestimation of flux for sources extended on scales comparable to the filter length. The exact flux loss for a particular source will depend on the size of the source along the scan directions, and will also depend on whether the peak surface brightness is above the 4σ threshold used in the second-level filtering. A simple simulation of a circular exponential disc shows that the filtering removes ∼50 per cent of the source flux if the diameter of the disc is equal to the filter length. If the diameter is half of the filter length, then only 5 per cent of the flux is removed. This suggests that sources with a diameter less than 1 arcmin should by relatively unaffected by the filtering. Flux measurements for sources larger than this should be treated with caution.

Fig. 4 compares the differential source counts calculated from the PACS SDP catalogues to those determined from the initial data of the complementary PACS Evolutionary Probe (PEP) survey (Berta et al. 2010), which is deeper than H-ATLAS but covers a smaller area. The good agreement between the two sets of counts supports the initial assumption that all bright PACS sources should already

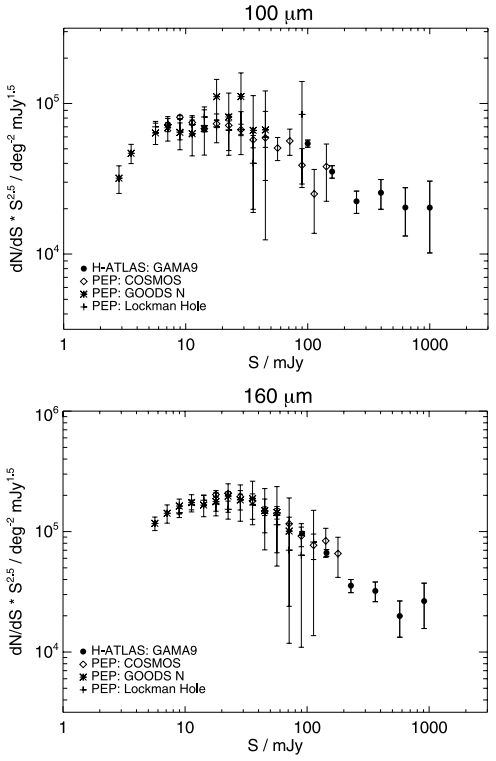

Figure 4. The differential source counts from the PACS section of the SDP catalogue compared to the initial results from the three fields covered by the PEP survey (Berta et al. 2010).

[3] See the scan mode release note, PICCMETN0.35.

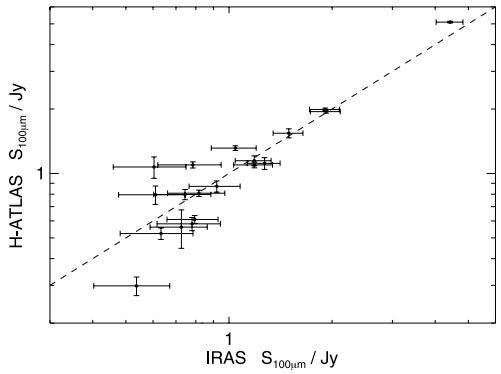

Figure 5. A comparison between the 100 flux densities from PACS and *IRAS*.

be present in the SPIRE catalogue. However, there are insufficient sources in the SDP data to properly constrain the bright number counts tail. A full analysis of the PACS counts will be presented in Ibar et al. (in preparation).

For the sources detected in the PACS 100 μm map an additional comparison can be made to this wavelength in the Imperial *IRAS*–FSC Redshift Catalogue of Wang & Rowan-Robinson (2009), which combines the original *IRAS* Faint Source Catalogue flux density values with improved optical and radio identifications and redshifts. There are 34 *IRAS* sources within the PACS region of the H-ATLAS SDP field; 19 of these have a reliable *IRAS* flux measurement and these are in good agreement with the SDP catalogue, with a mean offset consistent with zero, as shown in Fig. 5.

4 ASSESSING THE CATALOGUE RELIABILITY

4.1 Simulation creation

It is not enough to identify sources in the H-ATLAS SDP maps; the robustness of the catalogue must also be determined. This is done using realistic simulations of the observations, with the same noise properties as the processed maps, and a realistic cirrus background, based on *IRAS* measurements (Schlegel, Finkbeiner & Davis 1998). However, only the three SPIRE bands are considered in this initial analysis, as the PACS SDP catalogue is currently treated as an extension to the SPIRE data.

The simulated maps are randomly populated with sources generated using the models of Negrello et al. (2007), which predict the number counts of both the spheroidal and protospheroidal galaxy populations separately; for the simulations, these predictions are combined together to give the expected total counts, and hence the corresponding set of source flux densities, for each band. Although Maddox et al. (2010) detected, in SDP data, strong clustering for 350 and 500 μm selected samples, fluctuations due to faint sources at the SPIRE resolution are Poisson dominated, especially at 250 μm (e.g. Negrello et al. 2004; Viero et al. 2009). This suggests that, for the present purposes, using unclustered random positions is a sufficiently good approximation. The flux densities of all the sources in the models are reduced by 26 per cent at 250 μm and 15 per cent at 350 μm to improve the agreement with the observed (i.e. uncorrected) source counts in the SDP catalogue (Clements et al. 2010); the results of this alteration are shown in Fig. 6. The final flux density ranges are 0.11 mJy to 1.65 Jy at 250 μm, 0.24 mJy to 0.83 Jy at 350 μm and 0.45 mJy to 0.59 Jy at 500 μm for the

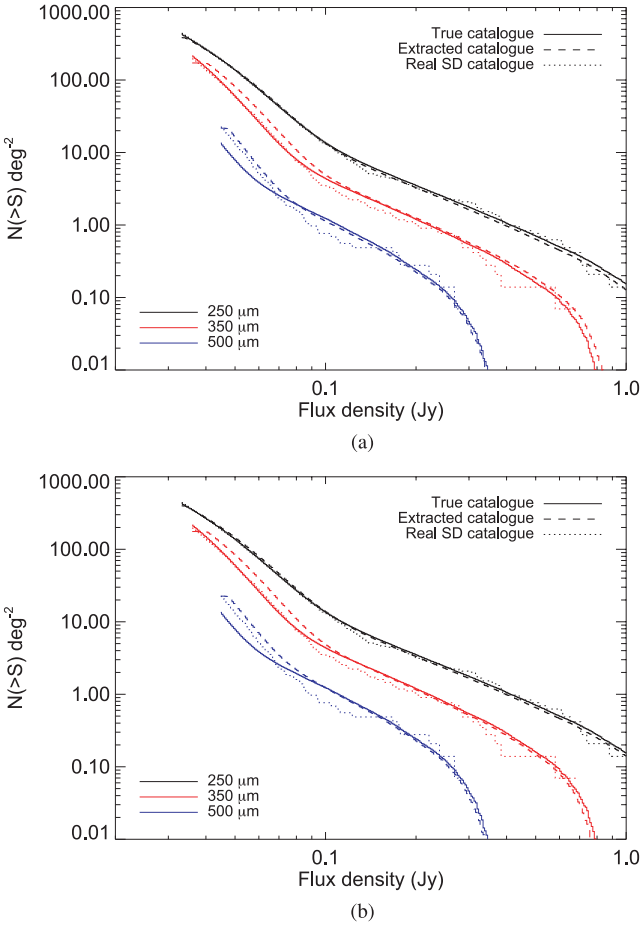

Figure 6. The integrated source counts from the combined set of 500 input (true) and extracted simulated catalogues, along with those calculated using the SDP catalogue for both versions of the simulations: (a) extended source simulations, (b) point source only simulations.

simulated sources; this ensures that the simulated maps contain a realistic background of faint sources which can contribute to the confusion noise.

The simulations are constructed by first adding the flux of each source in each band to the relevant position in a 1 arcsec grid. Two versions of the simulations are created. In the first the simulated sources are all one pixel in size (point source simulations: PSS),

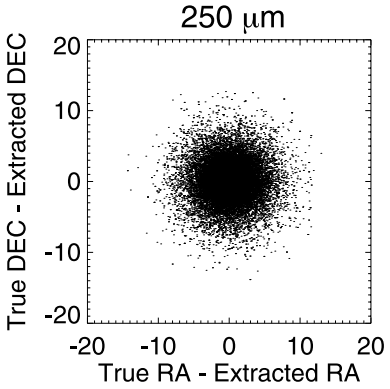

Figure 7. The positional offsets between the matched sources in the simulated extracted and input (true) full 250 μm catalogues. The results for the two versions are very similar, so only the PSS points are shown here.

whereas in the second the sources are assigned a scalelength based on their catalogue redshift [extended source simulations (ESS)]. The scalelength is constant in physical units, and then converted to an angular scale using standard cosmology. The ESS will obviously be a better representation of the real data, but, as Section 3.1.1 shows, MADX underestimates the flux densities of objects with sizes larger than the FWHM, so the PSS simulations provide a useful comparison. It should be noted that the flux densities and positions of the input sources will be the same in both cases. The next step is to convolve the 1 arcsec map by the appropriate *Herschel* PSF, also sampled on a 1 arcsec grid, to give a map of flux per beam covering the full area of the SDP data. Then, the 1 arcsec pixels are block averaged to give 5 arcsec pixels for the 250 μm maps, and 10 arcsec pixels for the 350 and 500 μm maps.

A background representing emission from Galactic cirrus is then added to each map. The background value is estimated from the Schlegel et al. (1998) map of 100 μm dust emission and temperature by assuming a modified blackbody spectrum with $\beta = 2.0$, and scaling to the appropriate wavelength. The resolution of this *IRAS* map is lower than that in the SDP data, which means that small-scale structure in the cirrus is not present in the simulations. Since the cirrus is highly structured, it is non-trivial to generate realistic structure on smaller scales, so as a simple approximation, the low-resolution maps were used, though it should be noted that the true cirrus background will include more small-scale features. It is clear that the real cirrus structure in the SDP data is highly non-Gaussian, so simply extrapolating the power spectrum to smaller scales does not significantly improve the model background.

Finally, instrumental noise is added to each pixel as a Gaussian deviate, scaled using the real coverage maps so that the local rms is the same as in the real data.

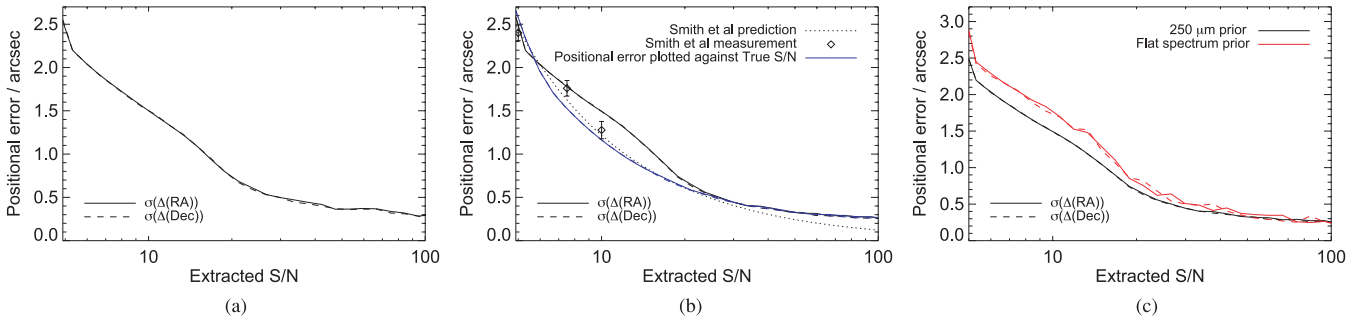

Figure 8. The positional errors for the two different versions of the simulations, alongside a comparison of the two different source extraction position priors as previously discussed in Section 3.1: (a) extended source simulations, (b) point source simulations, (c) point source simulations comparing different priors. Also shown in (b) are the positional errors plotted against the S/N in the input (true) catalogue, along with those determined by Smith et al. (2011) for the SDP data at 5, 7.5 and 10σ.

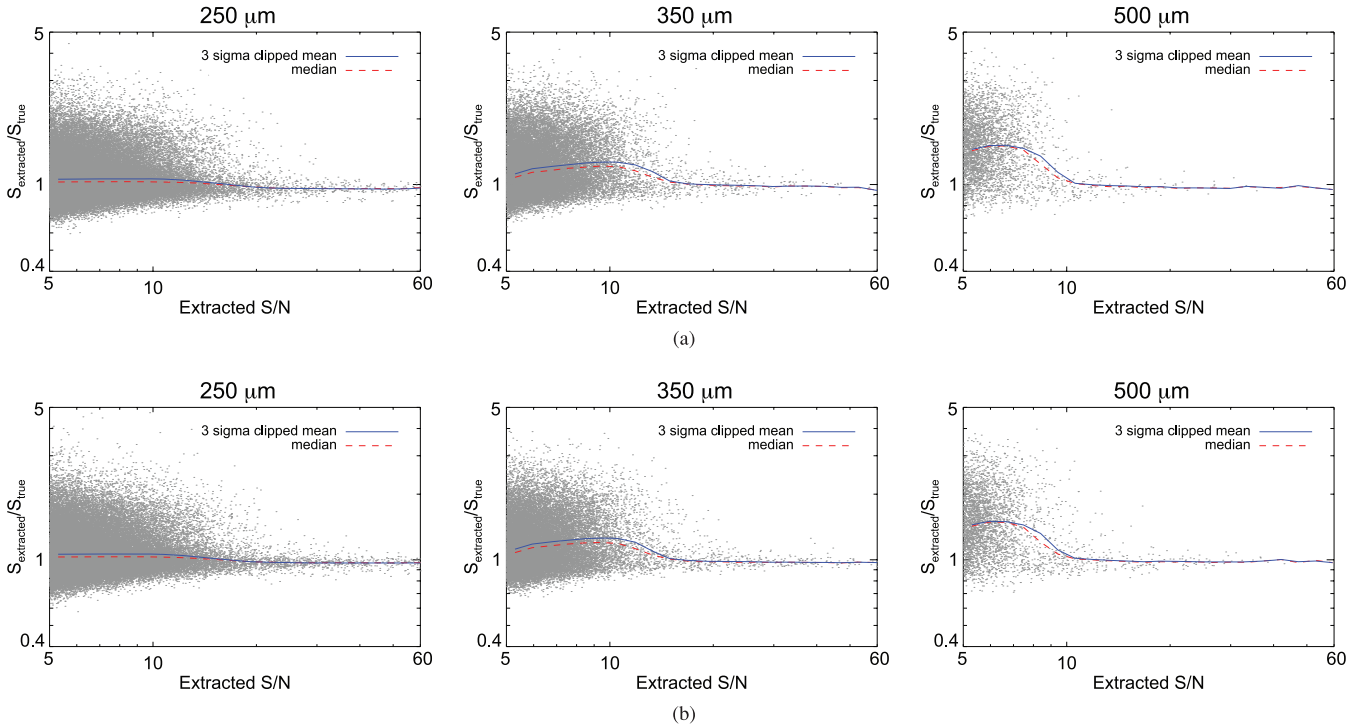

Figure 9. The ratio of flux densities for the matched sources in the simulated input (true) and extracted catalogues as a function of extracted S/N for the three bands from the ESS and PSS maps: (a) extended source simulations, (b) point source simulations. Also shown are the median and 3σ clipped mean values, calculated in bins of 0.05 in log(S/N).

Sources are then extracted with MADX from both versions of the simulations, following the procedure described in Section 3.1. For the ESS maps, the flux densities in the three bands are again replaced with aperture-measured values for the extended sources. The 'optical sizes' (needed to determine a_r using equation 1) in this case are taken as three times the scale-size taken from the input catalogues; this corresponds to a *B*-band isophotal limit of $\sim$25 mag arcsec^{-2} (Zhong et al. 2008). Finally, the MADX catalogue is cut to only include sources which are detected at the 5σ level in any of the available bands. This process is repeated 500 times, each time using a different realization of the input model counts, to ensure sufficient numbers of bright sources are present at the longer wavelengths. The average number of extracted sources which are also $>5\sigma$ in any band is 5881 and 5772 for PSS and ESS, respectively, which is lower than the 6876 sources present in the real SDP data; as Fig. 6 illustrates, this is because the simulated source counts do not exactly reproduce the real SDP ones. Additionally, more sources are found for the PSS version because of the flux underestimation of extended sources which means that the faintest objects fall below the catalogue cut. In the remainder of this discussion, these MADX catalogues will be referred to as the 'extracted catalogues', and the simulated input source lists as the 'simulated input catalogues'.

For each of the three bands in turn, starting with the brightest, sources in the extracted catalogue are matched to the simulated input source that makes the largest contribution, determined by weighting with the filtered beam, at that extracted position. A match radius of 3 pixels (approximately equal to the FWHM in each band) is also imposed to ensure that a match is not made to an unfeasibly distant source. Since the typical positional error for a $>5\sigma$ 250 μm source is 2.5 arcsec or less, this match radius will ensure that almost no real matches are rejected, whilst the weighting will avoid spurious matches. Once matched, a simulated input source is removed from consideration to avoid double matches. Considering each band separately will allow an extracted source to have three different simulated input counterparts, depending on where the majority of its flux density comes from at 250, 350 and 500 μm. This ensures that the effects of source blending in the data can be properly investigated, though it should be noted that the results are very similar if the counterparts are found at the highest resolution, shortest wavelength only. Full simulated input, extracted and matched catalogues for each band are then made by combining the results from the 500 individual sets of simulations together.

The positional offsets and corresponding errors are shown in Figs 7 and 8. They demonstrate that there is no significant offset between the extracted and matched catalogues. The positional errors for 5σ sources are $\sim$2.4 arcsec at 250 μm in both versions, which agrees with the value of 2.40 $\pm$ 0.11 arcsec found for the real SDP data by Smith et al. (2011). The errors also approximately scale as 1/(S/N) in the 250 μm band, as predicted by e.g. Ivison et al. (2007). However, at low S/N there is an enhancement over the predicted values, as illustrated for the PSS results in Fig. 8(b). This is a result of Eddington bias causing more faint sources errors to scatter up than vice versa; if the positional errors are plotted against the S/N in the simulated input catalogue, which does not suffer from this effect, then they are in better agreement with the prediction.

Table 1. The flux density correction factors (FC) at each SPIRE wavelength, as a function of S/N in the extracted catalogue, determined from the ratio of flux densities in the matched extracted and *simulated input* catalogues. To apply the correction at some catalogue flux density, f_{cat}: $f_{corr} = f_{cat}/FC$, though note that the density correction given in Table 2 should also be applied as well.

	ESS			PSS		
Catalogue S/N	$FC_{250\,\mu m}$	$FC_{350\,\mu m}$	$FC_{500\,\mu m}$	$FC_{250\,\mu m}$	$FC_{350\,\mu m}$	$FC_{500\,\mu m}$
5.30	1.06	1.12	1.45	1.06	1.12	1.45
5.94	1.06	1.18	1.51	1.06	1.18	1.50
6.67	1.06	1.21	1.51	1.06	1.21	1.50
7.48	1.06	1.23	1.47	1.06	1.23	1.45
8.39	1.06	1.25	1.35	1.06	1.25	1.32
9.42	1.06	1.27	1.14	1.06	1.26	1.11
10.57	1.06	1.27	1.01	1.06	1.25	1.02
11.86	1.05	1.23	1.00	1.05	1.20	1.00
13.30	1.04	1.15	0.99	1.04	1.10	0.99
14.93	1.02	1.04	0.98	1.02	1.01	0.99
16.75	1.00	1.01	0.98	1.00	0.99	0.98
18.79	0.98	1.00	0.98	0.98	0.99	0.99
21.08	0.97	0.99	0.97	0.98	0.98	0.98
23.66	0.96	0.99	0.97	0.97	0.98	0.98
26.54	0.96	0.99	0.96	0.97	0.98	0.98
29.78	0.96	0.98	0.96	0.97	0.97	0.98
33.42	0.96	0.98	0.98	0.97	0.98	0.98
37.49	0.95	0.98	0.97	0.97	0.97	0.99
42.07	0.96	0.98	0.96	0.97	0.97	1.00
47.20	0.95	0.97	0.99	0.97	0.97	0.98
52.96	0.95	0.97	0.96	0.97	0.97	0.99
59.43	0.96	0.94	0.95	0.97	0.97	0.97
66.68	0.95	0.93	–	0.96	0.97	–
74.81	0.95	0.92	–	0.97	0.97	–
83.94	0.97	0.93	–	0.97	0.97	–
94.18	0.97	0.94	–	0.96	0.97	–

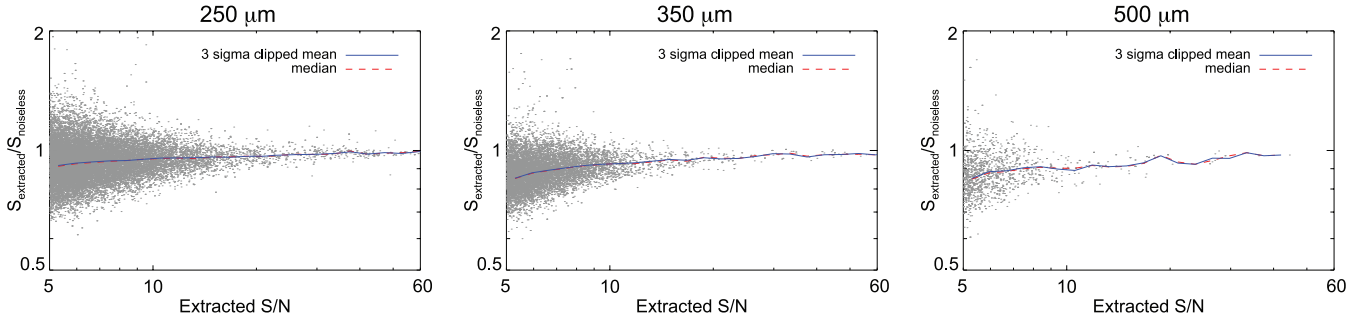

Figure 10. The ratio of flux densities for the matched sources in the noiseless MADX ($S_{noiseless}$) and extracted catalogues as a function of extracted S/N for the three bands (including point sources only). Also shown are the median and 3σ clipped mean values, calculated in bins of 0.05 in log(S/N).

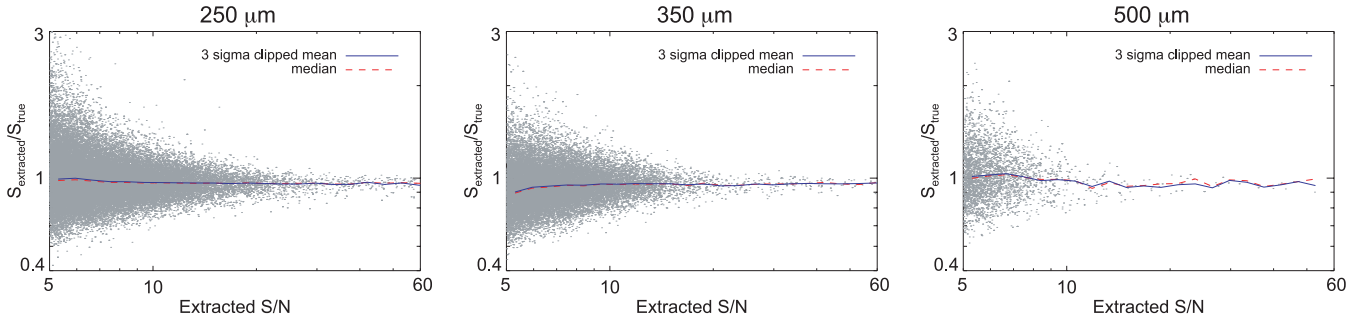

Figure 11. The ratio of flux densities for the matched sources in the simulated input (true) and extracted catalogues as a function of extracted S/N for the three bands, using the gridded position simulations (including point sources only). Also shown are the median and 3σ clipped mean values, calculated in bins of 0.05 in log(S/N). Note that confusion noise is not included in these simulations.

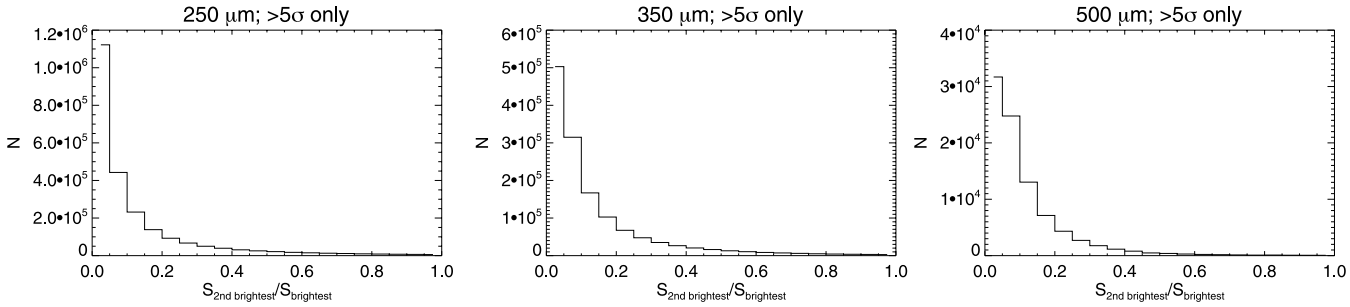

Figure 12. The PSF-weighted ratio of the brightest to the second brightest input (true) source contributing to the extracted source, within the beam in each band, for $>5\sigma$ sources in the extracted catalogue.

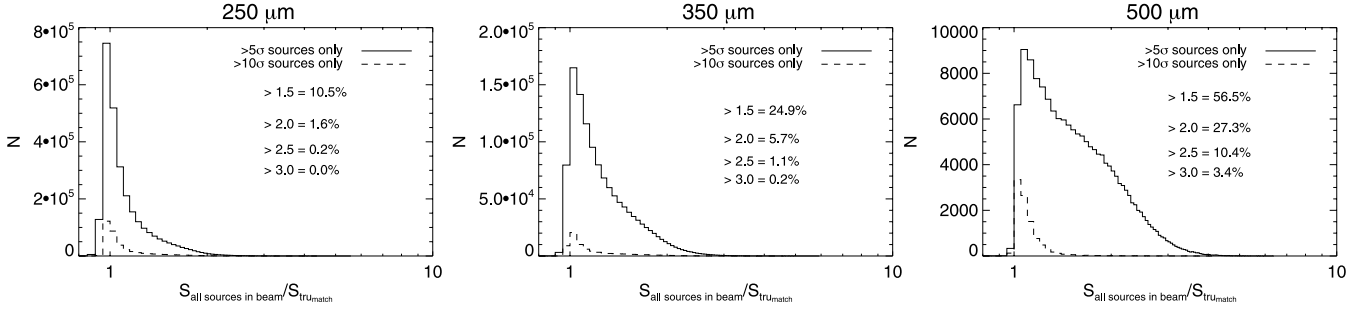

Figure 13. The PSF-weighted, background-subtracted, ratio of the sum of simulated input (true) sources within a beam to the flux density of the matched true source for $>5\sigma$ (solid line), and $>10\sigma$ (dashed line) sources in the extracted catalogue. The labels on the figures give the percentage of sources with ratios greater than some particular value. The small proportion of sources where the ratio falls below 1 is due to the PSF weighting.

Fig. 8(c) also illustrates the improvement in positional errors that arises from selecting sources at 250 μm only in MADX, instead of giving equal weight to all bands (flat-spectrum prior), as previously discussed in Section 3.1. Greater positional accuracy significantly enhances the efficacy of the cross-identification to optical sources using the Likelihood Ratio method (Smith et al. 2011). This is why the better positions are deemed to outweigh the slight chance of missing red objects when using the 250 μm prior.

4.2 Catalogue correction factors

Inspection of Fig. 6 shows a clear discrepancy between the extracted and simulated input integral counts at faint 500 μm flux densities; this occurs due to a combination of two factors. The first, flux-boosting, is a preferential enhancement of faint source flux densities due to positive noise peaks, that arises due to the steepness of the faint end (i.e. $S_{500\,\mu m} \lesssim 40$ mJy; Clements et al. 2010) of the source counts. The second is a result of blending, where several simulated input sources (which may be too faint to be included individually) are detected as one source in the extracted catalogue.

These effects can be quantified by direct comparison of the simulated input and extracted flux densities, shown in Fig. 9, as a function of S/N in the extracted catalogue for both the ESS and PSS versions. Flux correction factors are derived from the 3σ clipped mean of these data; these are given in Table 1. Applying these factors to each extracted source gives a statistically 'flux-corrected' catalogue. It should be noted, however, that the discussion of correction factors in this section is restricted to sources detected at a 5σ or greater level only.

An alternative approach to determining the catalogue correction factors is to use a 'noiseless' catalogue, created by running MADX on the simulated maps before the addition of noise, as the comparison. As Fig. 10 shows, this does not accurately represent the level of flux enhancement in the data, because the noiseless catalogue is also affected by source blending. Additionally, at low S/N the noiseless-input flux densities are generally brighter than the extracted ones, suggesting that MADX underestimates the background-subtraction in the absence of noise.

The relative contributions from the flux-boosting and source blending can be investigated with a new set of simulated, point source only, maps, in which the sources are placed on a regular spaced grid, with a 70 arcsec separation between points, to ensure no sources overlap. The source density is also lowered in these maps (imposed by excluding any source in the simulated input catalogue with a 250 μm flux density fainter than 6.6 mJy), so that sufficient unique positions can be generated. Inspecting the ratio of the extracted and simulated input fluxes (Fig. 11) suggests that the majority of the flux enhancement seen in Fig. 9 is due to blended sources, rather than boosting due to noise. However, the PSF-weighted ratio of the brightest to second brightest simulated input source contributing to each source in the extracted catalogue (Fig. 12) appears to contradict this; it shows that, even at 500 μm, blending with this second source would not increase the extracted flux density by the amount seen. The solution to this apparent contradiction becomes clear when the PSF-weighted ratio of the contribution from all the simulated input sources within a beam to the flux density of the simulated input match is considered instead (Fig. 13). Here, ∼27 per cent of 500μm $> 5\sigma$ extracted sources have sufficient simulated input sources available to boost their flux densities by a factor of 2 or more when their contributions are combined, even though their individual effect is small. Fig. 13 also shows that this confusion becomes negligible for $>10\sigma$ sources. This is in broad agreement with Chapin et al. (2011) who find that the sub-mm peaks they detect using a survey with larger beams, but of similar depth to H-ATLAS, generally consist of a blend of several sources. Future versions of MADX will include a deblending step which should reduce this effect. It should be noted that a mean sky-background of 6.8 mJy, 5.8 mJy or 4.1 mJy at 250 μm, 350 μm and 500 μm, respectively (determined from the mean of the simulated input catalogue), is subtracted before the histograms are calculated, to account for the background-subtraction carried out as part of the source extraction process.

As a check on the success of the correction factors in Table 1, they are applied to the full extracted catalogues and the

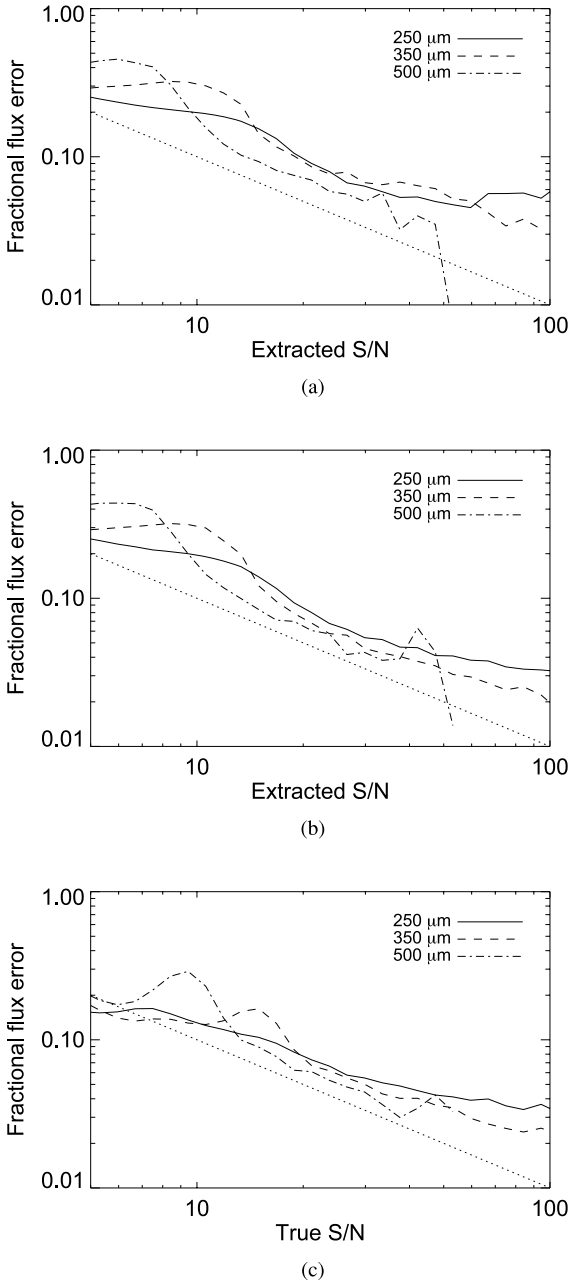

Figure 14. The fractional flux density error for the corrected, extracted catalogues, ignoring any sources that fall outside the 99.73rd percentiles: (a) extended source simulations, (b) point source simulations, (c) point source simulations. The dotted lines indicate the expected behaviour.

fractional flux density errors (after rejecting the points which lie outside the 99.73rd percentile) are then calculated. As Fig. 14 shows, these reduce with increasing S/N, but, as with the positional errors discussed previously, Eddington bias prevents this behaving exactly as expected. Again, when plotted against the S/N from the simulated input catalogue (Fig. 14c) the difference is reduced.

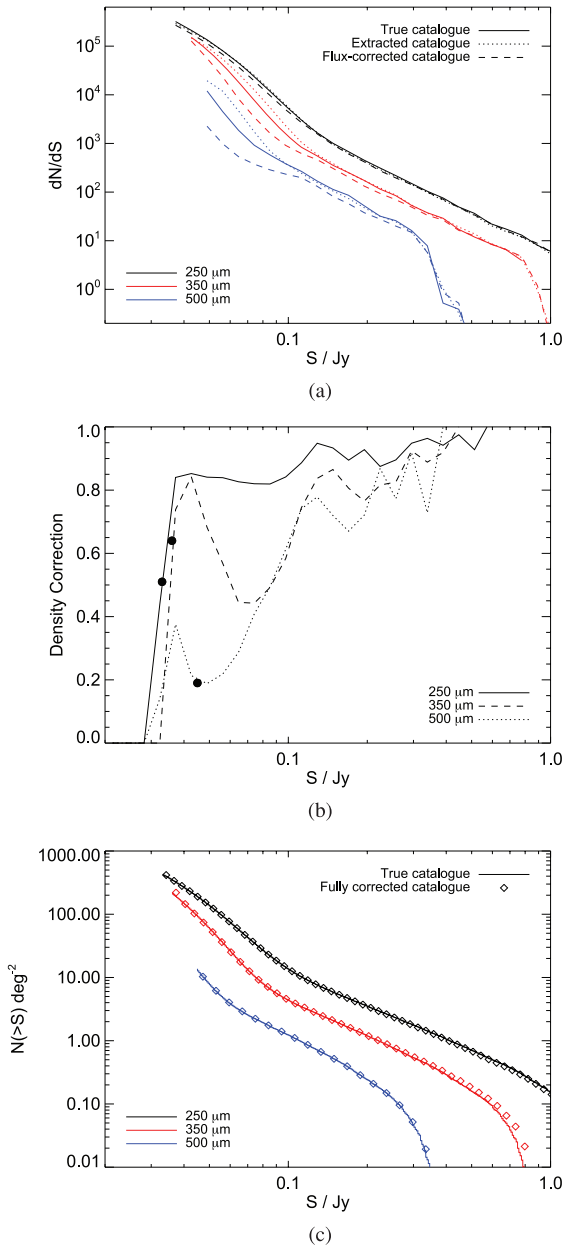

Figure 15. Extended source simulations. (a) The differential source counts for the extracted, simulated input (true) and flux–corrected catalogues for the three bands. Note the discrepancy between the flux–corrected and simulated input catalogues at faint flux densities. (b) The surface density correction required at each band to correct for the catalogue incompleteness, determined from the ratio of the flux–corrected to simulated input differential source counts. The solid dots indicate the position of the average 5σ limit in each band. (c) The integral source counts from the simulated input catalogue overplotted with the flux and surface–density corrected catalogue to demonstrate the success of these correction factors at recovering the simulated input values.

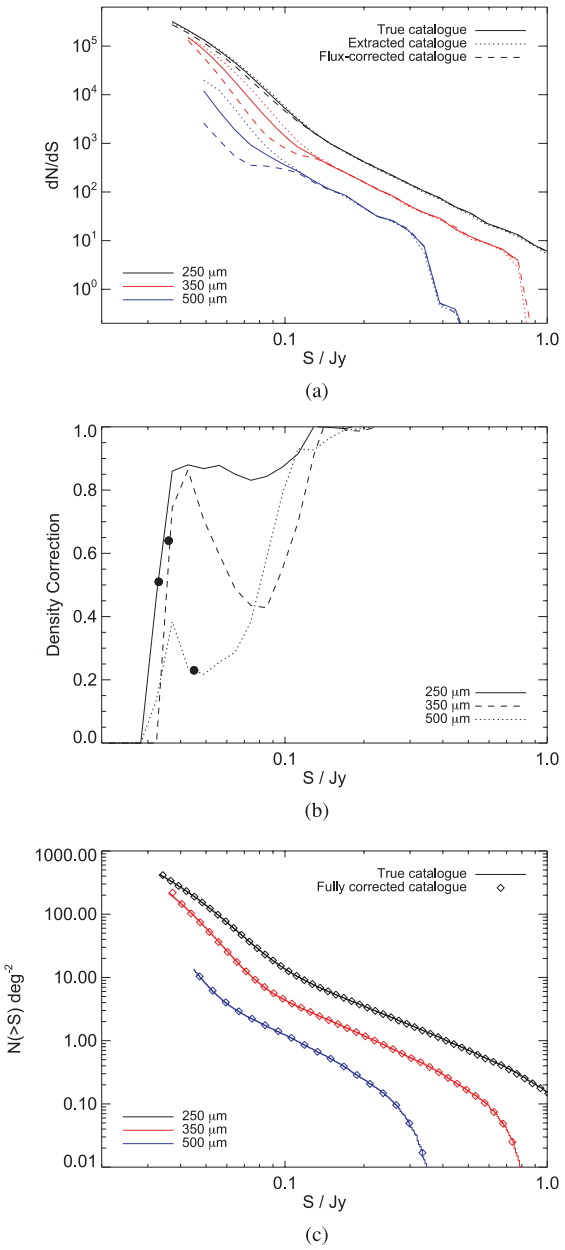

Figure 16. Point source simulations. (a) The differential source counts for the extracted, simulated input (true) and flux–corrected catalogues for the three bands. Note the discrepancy between the flux–corrected and simulated input catalogues at faint flux densities. (b) The surface density correction required at each band to correct for the catalogue incompleteness, determined from the ratio of the flux–corrected to simulated input differential source counts. The solid dots indicate the position of the average 5σ limit in each band. (c) The integral source counts from the simulated input catalogue overplotted with the flux and surface–density corrected catalogue to demonstrate the success of these correction factors at recovering the simulated input values.

As well as the flux correction factors, we also need to consider the completeness of the detected catalogues, especially at faint 350 and 500μm flux densities; this is clearly seen in Figs 15(a) and 16(a) which compare the differential source counts for the extracted, simulated input and flux-corrected catalogues. The lower counts are due to the failure to detect some fraction of faint sources because of random noise fluctuations in the simulated maps or source blending.

Table 2. The surface density correction (SC) at each SPIRE wavelength as a function of corrected flux density, determined from the ratio of the flux-corrected to *simulated input* differential counts. To apply the correction at some corrected flux density, $f_{\rm corr}$: $f_{\rm corr\_final} = f_{\rm corr}/{\rm SC}$. The corrected flux densities given are the central bin values.

Corrected flux density	ESS			PSS		
(Jy)	$SC_{250\,\mu m}$	$SC_{350\,\mu m}$	$SC_{500\,\mu m}$	$SC_{250\,\mu m}$	$SC_{350\,\mu m}$	$SC_{500\,\mu m}$
0.0320	0.31	–	–	0.40	–	–
0.0327	0.75	–	0.11	0.79	–	0.11
0.0335	0.84	–	0.41	0.85	–	0.39
0.0343	0.84	–	0.49	0.85	–	0.49
0.0351	0.83	–	0.48	0.85	–	0.48
0.0359	0.85	0.01	0.46	0.86	0.01	0.46
0.0367	0.84	0.68	0.39	0.86	0.71	0.41
0.0376	0.85	1.36	0.31	0.87	1.36	0.33
0.0385	0.83	1.36	0.26	0.86	1.36	0.27
0.0394	0.83	1.34	0.25	0.86	1.34	0.26
0.0403	0.85	1.07	0.25	0.88	1.11	0.27
0.0427	0.85	0.84	0.21	0.88	0.86	0.24
0.0490	0.84	0.68	0.19	0.87	0.71	0.22
0.0562	0.84	0.57	0.22	0.88	0.60	0.26
0.0646	0.83	0.45	0.29	0.85	0.49	0.29
0.0741	0.82	0.44	0.41	0.83	0.43	0.38
0.0851	0.82	0.49	0.49	0.84	0.43	0.59
0.0977	0.84	0.58	0.61	0.87	0.55	0.79
0.1122	0.89	0.74	0.74	0.92	0.70	0.93
0.1288	0.95	0.84	0.78	1.00	0.91	0.93
0.1479	0.93	0.87	0.72	1.00	1.05	0.96
0.1698	0.89	0.81	0.67	0.99	0.99	0.99
0.1950	0.93	0.77	0.72	1.01	0.99	0.99
0.2239	0.87	0.82	0.87	1.00	1.00	1.00
0.2570	0.90	0.83	0.77	1.00	1.00	1.00
0.2951	0.95	0.92	0.92	1.00	1.00	1.00
0.3388	0.96	0.89	0.73	1.00	1.00	1.00
0.3890	0.94	0.92	1.00	1.00	1.00	1.00
0.4467	0.98	1.00	1.00	1.00	1.00	1.00
0.5129	0.93	1.00	1.00	1.00	1.00	1.00
0.5888	1.02	1.00	1.00	1.00	1.00	1.00
0.6761	1.00	1.00	1.00	1.00	1.00	1.00
0.7762	1.00	1.00	1.00	1.00	1.00	1.00
0.8913	1.00	1.00	1.00	1.00	1.00	1.00
1.0233	1.00	1.00	1.00	1.00	1.00	1.00

This incompleteness can be quantified by simply taking the ratio of the flux-corrected to simulated input differential counts, to give a source–surface-density correction. Note that this is not appropriate for correcting the flux densities of individual sources, but rather it can be applied when making statistical analyses of the catalogue as a whole. This correction is shown in Figs 15(b) and 16(b), and also given as an additional correction factor in Table 2. Figs 15(c) and 16(c) demonstrate the success of the density correction when applied to the integral source counts.

There is one further factor that can affect the extracted catalogue – contamination from spurious sources. The expected number of $\geq 5\sigma$ random noise peaks present in the 250 μm map area is only ∼0.05, so this should be negligible in the SDP catalogue. Contamination from fainter sources which are boosted or blended is accounted for in the flux correction factors.

It should be noted that an alternative approach to correcting the SDP H-ATLAS catalogue was adopted in Clements et al. (2010). In this case corrections were determined from the ratio of extracted to simulated input integral source counts. This combines the effects of incompleteness and flux-boosting, and is appropriate for recovering the correct source counts, but not for correcting individual catalogue sources.

5 CONCLUDING REMARKS

This paper has presented the SDP catalogue for the first observations of the H-ATLAS, along with a description of the simulations created to determine the factors needed to correct it for the combined effects of incompleteness, flux-boosting and source blending. The main results of this analysis are summarized below.

(i) The extracted flux densities of 350 and 500 μm sources can be enhanced over their simulated input values, by factors of up to ∼2. This predominantly affects sources with $5 < {\rm S/N} < 15$.

(ii) These enhancements are shown to be due to source blending, with ∼27 per cent of $>5\sigma$ 500 μm sources having sufficient simulated input sources available within a beam to create a boosting of ∼2.

(iii) A combination of flux density and source–surface-density corrections is necessary to correct the extracted source counts for these factors.

It is anticipated that future development of the MADX software will incorporate subroutines to deal with both the effects of map pixelization and source blending in the processing stage.

MADX is not the only source extraction method being considered for the H-ATLAS data, but time constraints mean that it has been used for the SDP catalogue presented here. A comparison between different source extraction algorithms is currently ongoing; these include SUSSEXTRACTOR developed by Savage & Oliver (2007), as well as the 'matrix filter' method of Herranz et al. (2009) and the 'Mexican Hat wavelet' method of González-Nuevo et al. (2006) and López-Caniego et al. (2006). The results of this comparison will be used to improve future H-ATLAS catalogues.

This initial, uncorrected, catalogue will be available from http://www.h-atlas.org, though it is expected that as the data processing steps are refined it will undergo future updates.

ACKNOWLEDGMENTS

The *Herschel*-ATLAS is a project with *Herschel*, which is an ESA space observatory with science instruments provided by European-led Principal Investigator consortia and with important participation from NASA. The H-ATLAS website is http://www.h-atlas.org/1. The US participants in *Herschel*-ATLAS acknowledge support provided by NASA through a contract issued from JPL. The Italian group acknowledges partial financial support from ASI/INAF agreement n. I/009/10/0.

REFERENCES

Amblard A. et al., 2010, A&A, 518, L9
Baes M. et al., 2010, A&A, 518, L39
Berta S. et al., 2010, A&A, 518, L30
Chapin E. L. et al., 2011, MNRAS, 411, 505
Clements D. L. et al., 2010, A&A, 518, L8
Driver S. P. et al., 2009, Astron. Geophys., 50, 5.12
Dye S. et al., 2010, A&A, 518, L10
Eales S. et al., 2010, PASP, 122, 499
González-Nuevo J., Argüeso F., López-Caniego M., Toffolatti L., Sanz J. L., Vielva P., Herranz D., 2006, MNRAS, 369, 1603
González-Nuevo J. et al., 2010, A&A, 518, L38
Griffin M. J. et al., 2010, A&A, 518, L3
Herranz D., López-Caniego M., Sanz J. L., González-Nuevo J., 2009, MNRAS, 394, 510
Ibar E. et al., 2010, MNRAS, 409, 38
Ivison R. J. et al., 2007, MNRAS, 380, 199
López-Caniego M., Herranz D., González-Nuevo J., Sanz J. L., Barreiro R. B., Vielva P., Argüeso F., Toffolatti L., 2006, MNRAS, 370, 2047
Maddox S. J. et al., 2010, A&A, 518, L11
Negrello M., Magliocchetti M., Moscardini L., De Zotti G., Granato G. L., Silva L., 2004, MNRAS, 352, 493
Negrello M., Perrotta F., González-Nuevo J., Silva L., de Zotti G., Granato G. L., Baccigalupi C., Danese L., 2007, MNRAS, 377, 1557
Nguyen H. T. et al., 2010, A&A, 518, L5
Ott S., 2010, in Mizumoto Y., Morita K.-I., Ohishi M., eds, ASP Conf. Ser. Vol. 434, Astronomical Data Analysis Software and Systems XIX, Astron. Soc. Pac., San Francisco, p. 1390
Pascale E. et al., 2011, MNRAS, in press (doi:10.1111/j.1365-2966.2011.18756.x)
Pilbratt G. L. et al., 2010, A&A, 518, L1
Poglitsch A. et al., 2010, A&A, 518, L2
Savage R. S., Oliver S., 2007, ApJ, 661, 1339
Serjeant S. et al., 2003, MNRAS, 344, 887
Serjeant S. et al., 2010, A&A, 518, L7
Schlegel D. J., Finkbeiner D. P., Davis M., 1998, ApJ, 500, 525
Smith D. J. B. et al., 2011, MNRAS, in press (arXiv:1007.5260)
Thompson M. A. et al., 2010, A&A, 518, L134
Turin G., 1960, IRE Trans. Inf. Theor., 6, 311
Viero M. P. et al., 2009, ApJ, 707, 1766
Wang L., Rowan-Robinson M., 2009, MNRAS, 398, 109
Zhong G. H., Liang Y. C., Liu F. S., Hammer F., Hu J. Y., Chen X. Y., Deng L. C., Zhang B., 2008, MNRAS, 391, 986

This paper has been typeset from a TEX/LATEX file prepared by the author.